Investigation of the superelastic behavior of a Ti-16Zr-13Nb-2Sn sputtered film by nanoindentation

Y. Zhou, A. Fillon, H. Jabir, D. Laillé, T. Gloriant

PII: S0257-8972(20)31360-8

DOI: https://doi.org/10.1016/j.surfcoat.2020.126690

Reference: SCT 126690

To appear in: *Surface & Coatings Technology*

Received date: 15 November 2020

Accepted date: 27 November 2020

Please cite this article as: Y. Zhou, A. Fillon, H. Jabir, et al., Investigation of the superelastic behavior of a Ti-16Zr-13Nb-2Sn sputtered film by nanoindentation, *Surface & Coatings Technology* (2018), https://doi.org/10.1016/j.surfcoat.2020.126690

Investigation of the superelastic behavior of a Ti-16Zr-13Nb-2Sn sputtered film by nanoindentation

Y. Zhou, A. Fillon*, H. Jabir[1], D. Laillé, T. Gloriant

Univ Rennes, INSA Rennes, CNRS, ISCR-UMR 6226, F-35000 Rennes, FRANCE

[1] Present address: Laboratoire PIMM, UMR 8006, ENSAM – CNRS - CNAM, HESAM Université, F-75013 Paris, France

* Corresponding author at: Univ Rennes, INSA Rennes, CNRS, ISCR-UMR 6226, 20 avenue des Buttes de Coësmes, CS 70839, 35708 Rennes Cedex 7, France. E-mail address: amelie.fillon@insa-rennes.fr (A. Fillon).

Abstract

A new Ti-16Zr-13Nb-2Sn superelastic film incorporating β-stabilizing and highly biocompatible elements was elaborated by magnetron sputtering. The morphological, crystallographic and microstructural characteristics of the obtained films were studied by scanning electron microscopy, atomic force microscopy, X-ray diffraction, and transmission electron microscopy. Superelastic response of the film was investigated at local scale by nanoindentation using both spherical and Berkovich indenters. The sputter-deposited film revealed nanograined β microstructure with preferential growth orientation along [110] direction and excellent superelastic recovery at room temperature. Special attention was paid to the indenter geometry influencing reliable evaluation of the superelastic nature of the film. Evolution of the deformation mechanisms during nanoindentation at increasing depths was rationalized by the calculated representative strain beneath the indenting tips and is discussed in this work.

Keywords: Film; Sputtering; Ti alloys; Microstructure; Superelastic effect; Nanoindentation.

1. Introduction

Titanium (Ti) and its alloys have been extensively used as biomedical materials due to their high strength, low density, good corrosion resistance, low elastic modulus and high biocompatibility [1]. Some of these alloys can present shape memory effect or superelasticity [2]. Currently, superelastic NiTi alloy is widely used in biomedical applications as, for example, orthodontic archwires, self-expandable stents, abdominal wall lift devices, vascular ligation clips, or gastric loop snares [3]. NiTi presents unique superelastic performance and its recoverable strain can be as high as 10% [4]. However, owing to rising concerns over the hypersensitivity and toxicity of Ni element [5], research in superelastic alloys for biomedicine has shifted towards Ni-free metastable β-Ti alloys incorporating non-toxic and highly biocompatible elements (Nb, Zr, Hf, Ta, Sn) with the objective of optimizing their mechanical properties and superelastic performances.

Superelasticity refers to the property of recovering large deformation strain when removing an applied load. In metastable β-Ti alloys, superelasticity is attributed to the stress-induced martensitic transformation from the parent bcc-β phase to the orthorhombic-α″ martensite phase upon loading, and to the subsequent reverse transformation upon unloading resulting in remarkable accommodation of large reversible deformation strains [6]. Recently, the Ti-Zr-Nb-Sn bulk system has received much attention and appears promising alloy system for biomedical purpose because it

offers opportunity to combine large transformation strains, low elastic modulus and high strength by adjusting alloy concentration and optimization of microstructure, and also shows excellent cyto- and hemo-compatibility with enhanced viability and proliferation of living cells. For instance, Ti-(1~5)Zr-(12~17)Nb-(2~6)Sn [7-9], Ti-18Zr-(9~16)Nb-(0~4)Sn [10, 11], Ti-20Zr-12Nb-2Sn [12], Ti-24Zr-(8~12)Nb-2Sn [13] and Ti-(40~50)Zr-8Nb-2Sn [14] (at.%) bulk alloys have been reported in literature and some of which have reached superelastic recovery strain up to 7.5% at room temperature.

To our knowledge, there has been no reported work related to the Ti-Zr-Nb-Sn system in film geometries. Film technology is promising for further miniaturization and design possibilities for nanometer-sized functional tools and devices for biomedicine. In the field of superelastic films, most activities have focused on the superelastic response of magnetron sputtered NiTi-base alloy films since the 1990s, basically for the development of miniature systems (micro-sensors, -actuators, -pumps and -valves) [15-18]. Beside the suspected toxicity and carcinogenicity of nickel, a major drawback is the amorphous nature of as-deposited NiTi films at room temperature which required suitable heat treatment to obtain the crystalline phase responsible of the superelastic effect. Much less work has investigated superelastic response in Ni-free metastable β-Ti alloy films deposited by magnetron sputtered. One can mention some studies related superelasticity in Ti-Nb binary films [19], in Ti-(3~13)Zr-(18~23)Nb ternary films (at.%) [20] and in Ti-Nb-Ta-Zr quaternary films [21]. As with bulk alloys, it has been confirmed that superelastic response of ternary Ti-Zr-Nb films is much higher than that

of binary Ti-Nb films. Further studies were focused on microstructure and nanomechanical properties (elastic modulus and hardness) of magnetron sputtered Ni-free β-Ti alloy films, such as in Ti-Nb films [22-24] and in Ti-Nb-Zr films [25-27]. Magnetron sputtering offers the possibility to synthetize alloy films outside thermodynamic equilibrium enabling the formation of metastable phases in film geometries. Studies have confirmed that the allotropic β phase of Ti can be stabilized under the β transus temperature in β-Ti alloy films [28]. It has also been established that the addition of Zr as a substitute of Nb affects the lattice parameters of β phase and α'' martensite phase leading to an increase in the lattice deformation associated with the transformation strain during martensitic transformation which is beneficial for improving the accommodation of the deformation strain, and thus the superelastic response of alloys [20]. Meanwhile the decrease in Nb accelerates ω phase precipitation which affects superelasticity and increases drastically the elastic modulus and brittleness of alloys [24]. It has been observed that Sn addition suppresses ω phase formation and improves superelastic performances [29].

In the present work, we investigated if magnetron sputtered Ti-16Zr-13Nb-2Sn film could display superelastic properties as its bulk counterpart. In this Sn-added alloy film we suggested that full metastable β microstructure and large transformation strain could be obtained. For this purpose and considering previous work in bulk alloys [12], a new quaternary Ti-16Zr-13Nb-2Sn (in at.%) film was obtained by magnetron sputtering at room temperature and the morphological, crystallographic and microstructural characteristics of the films were investigated by scanning electron microscopy (SEM),

atomic force microscope (AFM), X-ray diffraction (XRD), and transmission electron microscopy (TEM).

Relatively little information is known about the reversible and stress-induced superelastic deformation at the micro- and nano-meter length scale in Ni-free Ti-based alloy films. Nanoindentation is considered as an efficient technique to characterize the locally nanoscale deformation behavior and mechanical properties of films because of its ability for characterizing mechanical response of small volume materials. Ma et al. [17] firstly used nanoindendation experiments in films to reveal the nanoscale superelasticity of NiTi films. The hysteresis loop of load-displacement indentation cycles was interpreted as the result of the occurrence of reversible and stress-induced martensitic phase transformation (i.e superelastic behavior). Wood and Clyne [30] demonstrated that nanoindentation, using the remnant depth ratio (unloaded depth /peak depth) as a detection parameter, was suitable for local testing whether or not superelastic deformation was occurring in NiTi alloys. A relatively low value for the remnant depth ratio was indicative that superelasticity was occurring. Moreover, the finite element method (FEM) simulations of the evolving strain fields under conical tip (which is considered to represent a good approximation to the Berkovich tip) and under spherical tip showed that peak strain levels are much higher under Berkovich indenter. Different indenter geometries make material exhibits different indentation responses. Nanoindentation experiment generates complex loading conditions necessitating considerable care in the interpretation of the nanoindentation responses. It was necessary to clarify which tip geometries and loading conditions were suitable to probe

superelastic recovery. Based on the studies of Liu et al.[31], Ni et al.[32], Achache et al.[19, 21] and Yang et al.[20], the work recovery ratio and depth recovery ratio extracted from indentation load-displacement (*F-h*) curves were able to probe the superelastic effect in bulk and film alloys. The higher values of work and depth recovery ratios especially during spherical indentation reflected the greater capability of the material to accommodate deformations and to behave more superelastically. Shastry et al. [33] described the variation of the depth recovery ratio with the calculated representative strain with a physically-meaningful and simple function, and showed the importance of selecting the appropriate representative strain window to capture the differences in depth recovery ratio between superelastic and shape memory behaviors of Ti alloys. The strain introduced into the material during Berkovich indentation was independent of penetration depth and caused significant plastic flow precluding a discriminating examination of the two different behaviors of Ti alloys. Spherical indentations, wherein the representative strain was varied systematically by changing the applied load, offered the advantage of investigating different deformation regimes from elastic to elasto-plastic to fully plastic regimes. Spherical indentations allowed to select the suitable representative strain window to reveal superelasticity and offered higher opportunity than Berkovich indentations to discern the discrepancies between two close behaviors in Ti alloys. In this study, nanoindentation technique was used to characterize the superelasticity of the obtained Ti-16Zr-13Nb-2Sn films, and four indenters with different geometry were used to study the nanoscale indentation behavior of superelastic Ti-16Zr-13Nb-2Sn films through different deformation regimes.

2. Materials and methods

2.1. Materials synthesis

The Ti-16Zr-13Nb-2Sn (at. %, Ti16132 for short) films were deposited on Si (100) substrates by radio frequency (RF) magnetron sputtering from a single target. Ultra-pure raw metals of titanium (>99.95 wt.%), zirconium (>99.078 wt.%), niobium (>99.9 wt. %) and tin (>99.99 wt. %) were used to synthetize the four-element ingot by the cold crucible levitation melting technique (CCLM). The ingot was next cold rolled and machined to obtain the alloyed target with perfect flat surface (76 mm diameter and 3 mm thick). The alloyed target was then cleaned in HF/HNO_3 solution (1/1 ratio). Si substrate was ultrasonically cleaned in acetone and ethanol for 5 min in each, and dried under compressed air gas, then mounted on the sample holder at a distance of 5.5 cm from the target. The chamber was evacuated to a base pressure of 3.4×10^{-5} Pa. High purity argon was used as the sputtering gas and the working pressure was maintained at 0.2 Pa. Before each deposition, the target was pre-sputtered in Ar plasma for 10 min to clean the target surface and to equilibrate thermally. During this stabilizing period the substrate was protected by a large shutter. During deposition at room temperature, the sputtering RF power of the target was fixed at 300 W and the negative voltage on the target was recorded as 385 V. Deposition was carried out for 50 min. Plane-view TEM specimen were also prepared by depositing thin film layer on a Cu TEM grid within a reduced time leading to a film thickness of 30 nm. Ti16132 coatings were studied in their as-deposited state without any post-treatment.

2.2. Microstructural and superelastic characterizations

Morphological and microstructural analyses were carried out on a JEOL JSM 6400 SEM operated at 10 kV. The chemical compositions of the composite target and films were assessed by energy dispersive X-ray spectroscopy (EDS) coupled with the SEM. 3D-topography and surface roughness were characterized using a Bruker Nano GmbH AFM operating in the tapping mode. Phase identification was performed using a Bruker D8 Advance XRD system in θ-2θ Bragg-Brentano mode with Cu-$K_{\alpha 1}$ radiation and power fixed at 40 kV and 40 mA. [110] pole figure of β phase was measured by XRD on Rigaku SmartLab Studio II system using Cu-$K_{\alpha 1}$ radiation at 40kV and 50 mA. TEM analyses of the plane view specimen were performed using a JEOL 2100 microscope operating at 200 kV.

Superelastic response of the Ti16132 film was investigated by nanoindentation using the instrumented NHT Anton Paar nanoindentation test system. Four indenter tips were used to explore the contribution of the superelastic response during the deformation of small volumes in our film: the Berkovich (Bkv) indenter and three spherical indenters with tip radii of 10 μm (Sp10), 50 μm (Sp50) and 200 μm (Sp200). There is a special interest in indenting with different indenter geometries for characterizing the superelasticity, because not all geometries developed strain states that predominantly induced the martensitic phase transformation. The penetration depth was kept in the first 10% of the film thickness to minimize the influence of the substrate material in the characterization of superelasticity. The depth recovery ratio η_h and work recovery ratio η_w were calculated from load-depth (*F*-*h*) nanoindentation curves to

evaluate the superelastic ability of Ti16132 film. The depth recovery ratio η_h is defined as:

$$\eta_h = \frac{h_m - h_p}{h_m} \quad (1)$$

where h_m is the maximum penetration depth at maximum applied load, and h_p is the permanent depth upon complete unloading [32]. The work recovery ratio η_w is defined as the ratio of recoverable work W_{rc} to the total work W_t:

$$\eta_W = \frac{W_{rc}}{W_t} = \frac{\int_{h_p}^{h_m} F.dh}{\int_0^{h_m} F.dh} \quad (2)$$

where W_{rc} is represented by the area enclosed by the unloading curve and the maximum penetration depth and W_t is represented by the area enclosed by the loading curve and the maximum penetration depth [31]. Relatively high values for η_h and η_w indicate the occurrence of superelastic effect [30].

Both η_h and η_w ratios of Berkovich indentations were found largely depth independent in many studies and it was recognized that the imposed strain during nanoindentation with sharp indenters, such as Bkv indenter, was independent of indentation depth and solely dependent on the indenter geometry [34]. Indeed, for a pyramidal indenter like Bkv tip, the ratio of the length of contact diagonal to the depth of penetration remains constant for increasing indenter load. Thus for ideally sharp pyramidal, the representative strain ε_r introduced into the material is determined by the face angles, as given according to Tabor's theory by the following relation:

$$\varepsilon_r = 0.2 \cot(\beta) \quad (3)$$

where β was the semi-apex angle of an axisymmetric equivalent cone [35]. For the Bkv indenter, β = 70.3° based on the equivalent displaced volumes in a single cone indenter

[36]. Hence, a representative strain of ~0.07 is found for the Bkv indenter.

For spherical indentations, the radius of the circle of contact increases faster than the depth of penetration as the load increases. Therefore, for spherical indenter, the representative strain ε_r is not constant and increases continuously with the area of contact as given by :

$$\varepsilon_r = 0.2\, a_c/R \quad (4)$$

where a_c is the in-plane contact radius and R the indenter radius. The contact radius a_c is defined from the geometry of indentation of a plane surface with a spherical indenter as $a_c=\sqrt{(2h_cR-h_c^2)}$, where h_c is the contact depth calculated from F-h indentation curves as per the following relation $h_c=h_m-0.75(F_m/S)$, where F_m is the maximum load and S is the stiffness estimated from the unloading curve using the Oliver–Pharr method [37]. The same value of representative strain may be obtained with different radii of spherical indenters and different depths. Spherical indentations offer the opportunity to vary the representative strain by changing either h_m with fixed R or R at a fixed h_m, enabling exploration from elastic to elasto-plastic deformation regimes. It is therefore expected that both η_h and η_w ratios of spherical indentations are depth-dependent. In this work, the representative strain ε_r was used to present the evolution of the measured indentation response through different deformation regimes.

3. Results

3.1. Microstructural properties

The chemical compositions of the alloyed target and film are given in Table 1. The Zr concentration in film was observed to be lower to that of the target. Only 15.6 at.%

of Zr was measured in the film whereas 19.7 at.% was found in the target. Compositions of the other elements of the film were observed to be very close to those of the target. The deviation in chemical composition between film and target is frequently attributed to the preferential sputtering effect. For film magnetron sputtered from an alloyed target, its composition depends greatly on the individual sputtering yields (the number of sputtered atoms per incident ion) of target components as well as their different masses [38]. Atoms of higher sputtering yield are removed preferentially from the bombarded surfaces resulting in surface segregation of one component. However, the reason for this depletion in Zr content in our film was not clear because it was expected that Zr and Nb elements which present similar sputtering yields, heats of sublimation and atomic weights would exhibit very close behaviors during the sputtering process [39, 40].

Table 1. Chemical compositions (in at. %) of the bulk target and the as-deposited film.

(at. %)	**Zr**	**Nb**	**Sn**	**Ti**
Target	19.7	12.1	1.9	balance
Film	15.6	13.5	1.7	balance

The cross-sectional SEM image and 3D AFM morphology of the film surface are shown in Fig. 1. The film thickness measured from cross-sectional images was uniform and estimated to be 3.3 μm. The film appeared extremely compact with no discernible morphological features indicating sufficient adatom surface mobility in consistence with the low deposition pressure (0.2 Pa). The SEM micrographs of plane view surfaces of the film (not presented here) displayed a very smooth surface with no discernible

morphological features. The surface morphology of the film observed by AFM displayed very small topographic features with uniform and fine needle shapes. The average roughness established from AFM images over a surface region of 5 µm x 5 µm was low at a value of 1.2 nm for the Ra roughness and 1.5 nm for the RMS roughness.

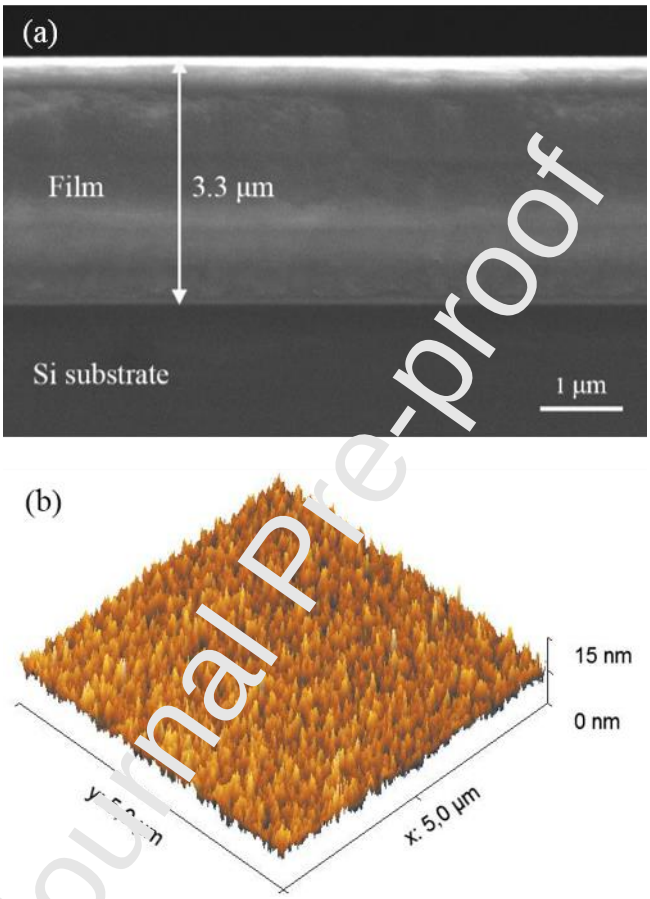

Fig. 1. (a) The cross sectional SEM image and (b) 3D AFM morphology of the Ti16132 film deposited on Si (100) substrate.

The XRD pattern, shown in Fig. 2, indicated that the film has a single β (bcc) phase structure. Formation of the high temperature β solid solution is common in Ti alloy films deposited via magnetron sputtering [19, 22, 24, 26]. Only the (110) and (220) diffraction peaks were observed indicating a strong fiber texture associated to preferential growth along the [110] direction with {110} dense planes lying parallel to

the substrate surface, as confirmed by the {110} pole figure shown in the insert of Fig. 2. There is a tendency for films grown by physical vapor deposition to develop specific preferred orientation which depends on the prevailing conditions during the deposition process including thermodynamic and kinetic considerations [41, 42]. The preferred orientation results from the competition between the strain and surface energies, and from the bombardment and mobility of incoming species at the film surface during growth process. In bcc alloys, {110} planes are the densest planes and have the lowest surface energy. The development of the [110] preferred orientation in our bcc film is determined by the minimization of the total surface energy. This behavior has been reported in binary Ti-Nb [19], ternary Ti-Zr-Nb [24, 26, 27] and quaternary Ti-Nb-Zr-Ta [21] films. The lattice parameter of the β phase calculated from the position of the diffraction peaks is 3.39 Å very close to that of the bulk alloy [10].

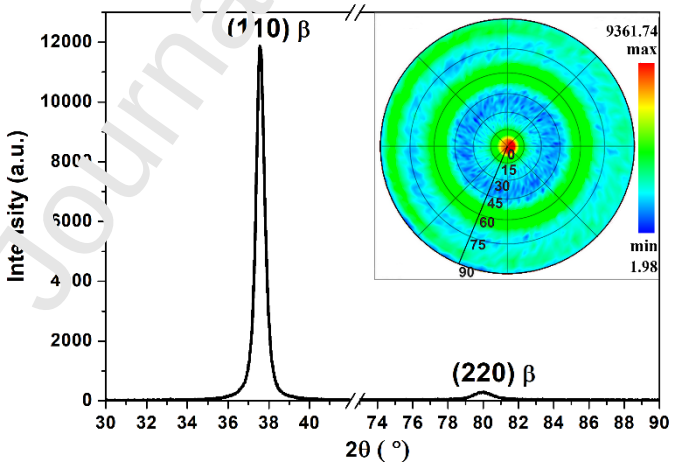

Fig. 2. XRD θ-2θ diffractogram of the Ti16132 film deposited on Si (100) substrate and the {110} pole figure in insert.

Fig. 3 shows the bright-field (BF) and high resolution (HR) TEM images from the plane-view specimen (30 nm thick) deposited on Cu grid. The BF-TEM image revealed

nanosized grains typically less than twenty nanometer diameter. The selected area electron diffraction (SAED) pattern associated to the BF-TEM image and inserted in the corner of Fig. 3(a), displayed continuous diffraction rings corresponding to the bcc-β phase and indicating the random orientation of the grains in the plane parallel to the substrate surface and the polycrystalline nature of the film. (110) planes were indexed according to the measured interplanar distance from the observable lattice fringes in the HR-TEM image (Fig. 3(b)). TEM observations confirmed that the film structure is fully β phase.

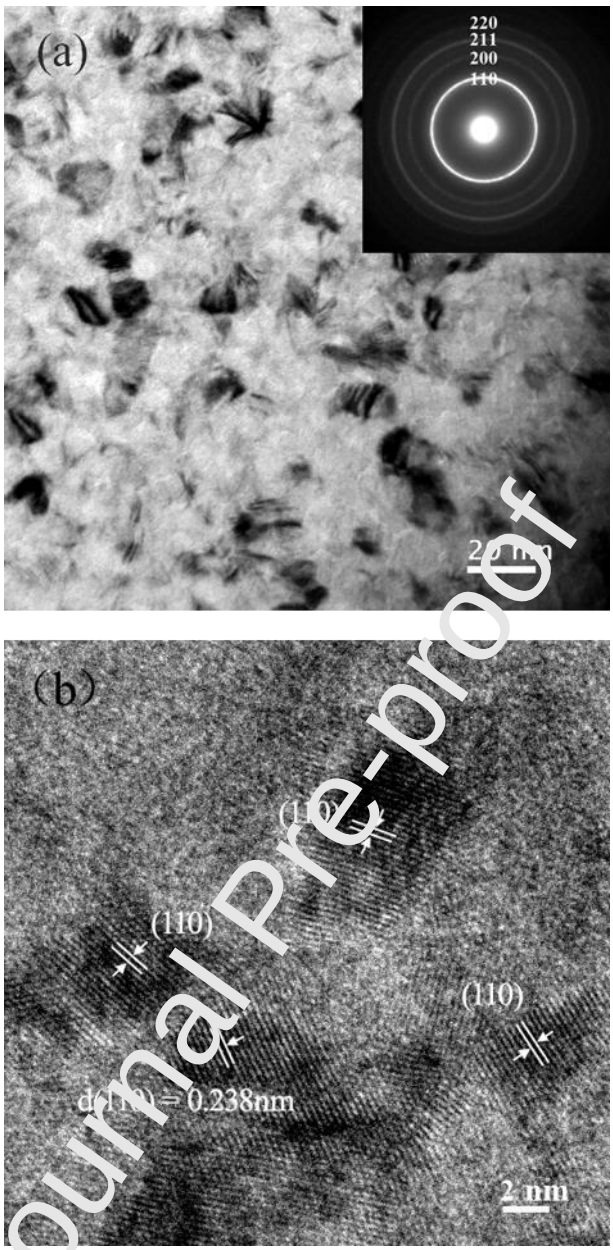

Fig. 3. TEM micrographs of the plane view specimen (30 nm thick) deposited on TEM Cu grid: (a) the bright-field (BF-TEM) image with the corresponding SAED pattern and (b) the high-resolution (HR-TEM) image.

3.2. Superelastic properties

Fig. 4 shows four sets of normalized *F-h* curves obtained from nanoindentations of Ti16132 film at three selected maximum depth h_m of 110 nm, 200 nm and 280 nm and for the three spherical indenters Sp10, Sp50 and Sp200 and for the Bkv indenter.

Normalized *F-h* curves were obtained from raw *F-h* curves by scaling the load and depth by their respective maximum load F_m and maximum indentation depth h_m. Thus, the non-dimensional *F-h* representation gives more sensitivity to unloading curves and allows a direct reading for η_h ratio as shown in Fig. 4(d). Normalized *F-h* curves allow to emphasize the depth dependence of η_h and η_w ratios.

The normalized *F-h* curves for Sp200 indenter (Fig. 4(a)) show that nearly complete recoveries were achieved whatever the maximum penetration depth indicating that elastic deformation of parent β phase predominates under these loading conditions. It may also indicate that the large radius of Sp200 tip is rather unwieldy that cannot stimulate and probe superelasticity in the film. When the intermediate (Sp50) and small (Sp10) spherical indenters were used, the normalized *F-h* curves (Fig. 4(b)-(c)) showed large recovery and depth dependence which is a characteristic of the occurrence of superelastic deformation. As mentioned earlier, for spherical indentations at equivalent penetration depths, the representative strain increases with the narrowness of the tip, and more accurately, it increases continuously with the area of contact between the tip and the film (Eq. (4)). The different tip radii offer the opportunity to vary the magnitude and the spatial distribution of the stress and strain fields for equivalent h_m. Moreover, it is recognized that superelastic performance is very sensitive to the applied strain level. The highest superelastic recovery strain in a given material is generally obtained for a narrow range of applied strain [14]. Those aspects confirm that nanoindentation equipped with appropriate indenters is a promising method for revealing whether or not the material can exhibit superelastic deformation and recovery.

For Bkv indentations, relatively limited recovery and very little depth dependence of normalized *F-h* curves were observed (Fig. 4(d)). This is attributed to the fact that the indentation response is dominated by the high strain immediately developed beneath the Bkv tip even at low applied loads, which is well beyond the strain levels that can be accommodated by superelastic deformation [30]. A sharp indenter will induce a fixed and large strain, which is independent of the depth of penetration (Eq. (3)). Under such condition, superelasticity is not expected to be possible.

The phase transformation behavior occurring during nanoindentation at nanometer scales is strongly dependent on local microstructural variations such as grain boundaries and crystal orientation [43]. In our nanocrystalline film, grain sizes are relatively small compared to the indent size and grains have the unique and common [110] orientation along the loading direction. Therefore, indentation responses of all indents presented in this work are supposed to be equally affected by grain boundaries and crystal orientation. In this way, mechanical features of our film were obtained from a very small and locally homogenized volume at microscale.

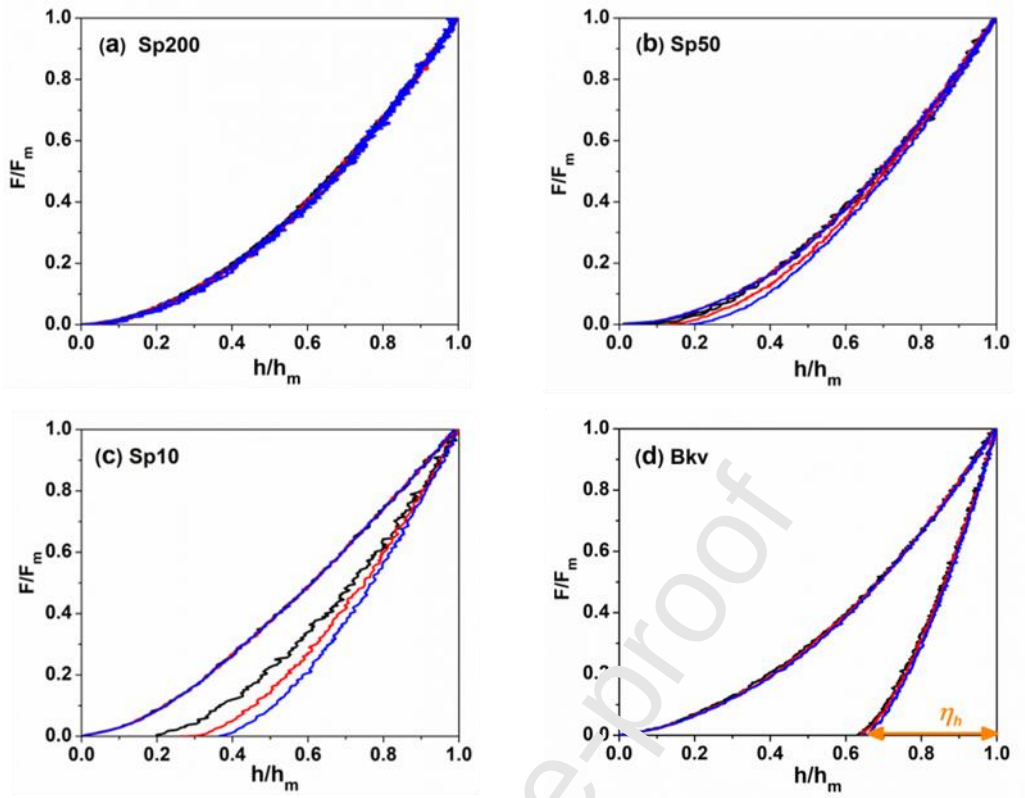

Fig. 4. Normalized load-displacement (*F*-*h*) curves obtained during nanoindentations carried out at three different maximum depths h_m of 110 nm (in black), 200 nm (in red) and 280 nm (in blue) using spherical indenters with different radii: (a) 200 µm (Sp200); (b) 50 µm (Sp50); (c) 10 µm (Sp10) and (d) using the Berkovich (Bkv) indenter.

To further investigate the influence of indenter geometry and the influence of maximum penetration depth h_m on the superelastic response, a series of nanoindentation experiments at various h_m ranging from 50 nm to 330 nm were performed on Ti16132 film with the three spherical indenters Sp200, Sp50, Sp10 and with the Bkv indenter. The depth recovery η_h and work recovery η_w ratios were calculated as described earlier (Eq. (1) and Eq. (2)) and plotted in Fig. 5 as a function of h_m for the four indenters. For a given h_m, Ti16132 film exhibited higher depth and work recovery ratios under spherical indenters compared to those measured under Bkv indenter. The highest η_h and

η_w ratios were observed with the Sp200 indenter, indeed values were nearly 100% for all h_m. In contrast, the decline in η_h and η_w ratios with h_m was more marked for Sp50 and Sp10 indenters. Recovery ratios ranged from 95% to 81% with Sp50 and from 85% to 60% with Sp10 for h_m ranging from 50 nm to 330 nm. Such depth dependence of recovery ratios was also reported for spherical indentations of superelastic NiTi alloys using FEM modeling and nanoindentation experiments [32, 44]. As expected, higher recovery values were obtained for the larger tip since the strain generated beneath spherical tip decreases with increasing tip radius. For Bkv indenter, η_h and η_w ratios were far below the values measured for spherical indenters. Recovery ratios remained below 50% and stabilized at 37% and 40% for η_h and η_w respectively when h_m exceeded 140 nm. Indeed, the high strain levels generated immediately beneath the Bkv tip even at low applied loads promote conventional plastic deformation via dislocation motions which in exchange limit the formation of martensite upon loading and inhibit its reversion upon unloading. Ni and al. already observed that recovery ratios of Berkovich indentations at various h_m are depth independent [32]. The slightly higher values of recovery ratios measured at shallow depths during Berkovich indentation can be attributed to a tip bluntness effect owing to the spherical end of the Bkv indenter tip [45]. The actual end shape of the Bkv indenter is not an ideally sharp triangular pyramid but typically exhibits a spherical end shape with a radius of curvature generally valued at around 100-150 nm [45, 46] and the repeated use aggravates the bluntness effect. Thus, when indentation depth is quite small and comparable to the tip radius of the apex, Berkovich indentation closely approaches the spherical indentation in nature,

demonstrating a depth dependence of recovery ratios as spherical indentations do. However, when the indentation depth exceeds the tip radius of the apex of Bkv indenter, the tip bluntness effect becomes insignificant and Berkovich indentation retrieve the sharp indenter properties with constant recovery ratios.

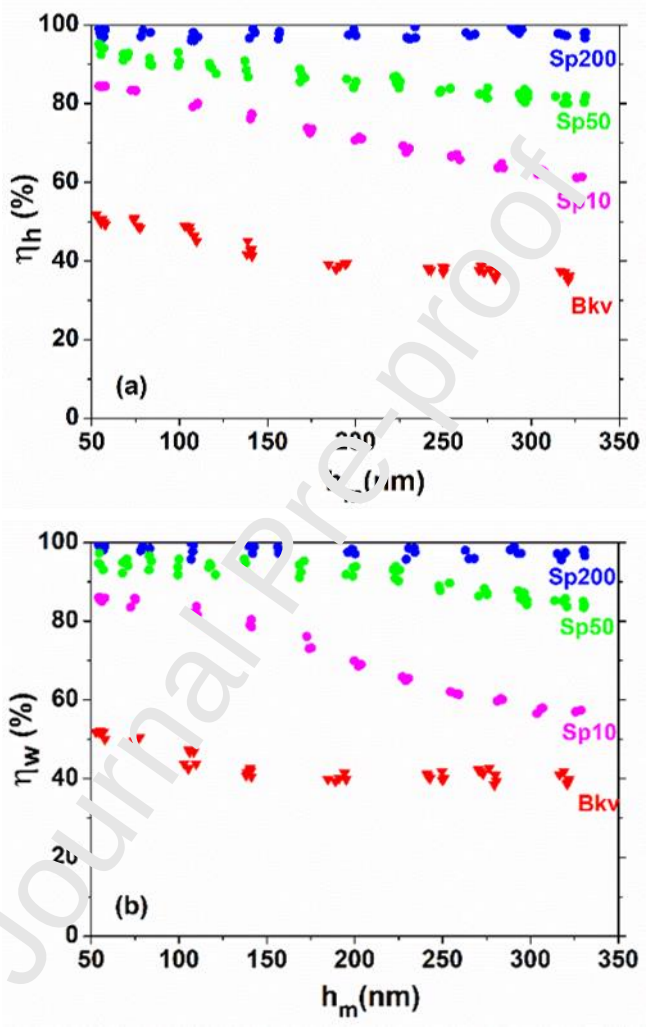

Fig. 5. Recovery ratios versus maximum indentation depth h_m for the three spherical indenters Sp200, Sp50 and Sp10 and for the Bkv indenter: (a) depth recovery ratio η_h and (b) work recovery ratio η_w.

4. Discussion

The different nanoscale indentation responses obtained from the various tip

geometries and at various h_m can be discussed in terms of imposed strain levels beneath the indenters. For that, the representative strain ε_r introduced into the film was calculated for each indenter used in this work using the formulae introduced earlier (Eq. (3) and Eq. (4)) and was plotted as a function of h_m in Fig. 6. The plot illustrates that ε_r depends greatly on the tip geometry. The shaper tip, the higher ε_r, which is also consistent with the predicted strain fields calculated from FEM simulations [30]. The bluntest Sp200 indenter generates the lowest ε_r from 0.4% to 0.5% for h_m ranging from 50 nm to 330 nm, followed by the intermediate Sp100 indenter and the small Sp10 indenter for which ε_r values range from 0.7% to 1.9% and from 1.6% to 4.3%, respectively, for h_m ranging from 50 nm to 330 nm. It can be seen that the ε_r under spherical indenters is far lower than that under ideally sharp Bkv indenter for which ε_r is considered depth independent and estimated to be around 7%. As mentioned above, actual Bkv indenter typically exhibits a spherical end tip with a radius of approximately 100-150 nm, which represents the smallest and the sharpest tip radius when compared with those of the three spherical indenters used in this study. In this case, it is reasonable to conclude that ε_r is much higher under the sharp Bkv tip. Moreover, calculation of ε_r is, in some way, an average value of the imposed strain beneath the indenter tip and it is also well established that the spatial gradations of stress and strain fields in the material underneath a sharp indenter such as the Bkv tip is much steeper than in the case of spherical indenters [30]. Therefore, it is generally considered that Berkovich geometry produces very localized high stress and high strain regions within the material underneath the tip. Using FEM modeling, Ni and al. showed that the maximum

equivalent plastic strain under ideally sharp pyramidal indenter is approximately three times higher than that under spherical indents at equivalent ε_r of 8% [32]. Considerable differences exist in the magnitude and spatial distribution of stress and strain fields between the spherical and pyramidal geometries [30]. In selecting different indenter shape and size, it is possible to investigate the nanoscale indentation behavior of small volumes of material over a wide range of representative strains (from 0.4% to 7% in the present work).

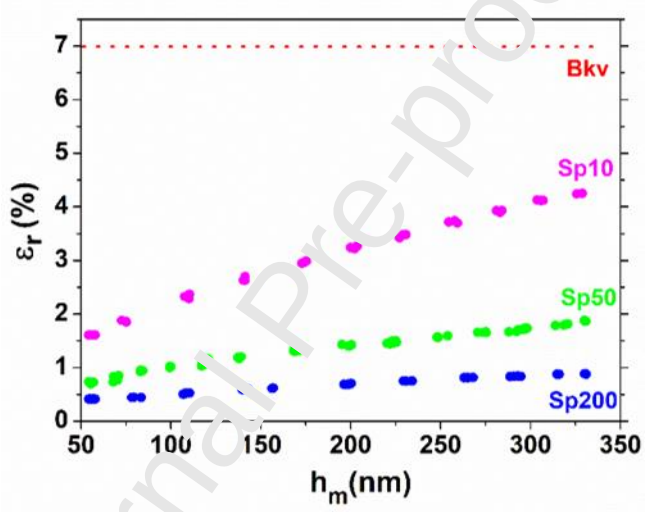

Fig. 6. Plot of the representative strain ε_r as a function of h_m for the three spherical indenters Sp200, Sp50, Sp10 and for the Bkv indenter.

Fig. 7 presents the measured η_h and η_w recovery ratios as a function of the calculated ε_r. It is evident that recovery ratios decrease with the strain level. For small strains, $\varepsilon_r \leqslant 1\%$, nearly 100% recoveries were obtained during spherical indentations with Sp200 indenter. As ε_r increases, recovery ratios decrease continuously from 95% to 60% for ε_r between 1% and 4.3% during spherical indentations with Sp50 and Sp10 indenters, and even decrease to 40% for ε_r of 7% during Berkovich indentations. One

can note the break on the X-axes of Fig. 7 to place the recovery ratios measured with Bkv indenter.

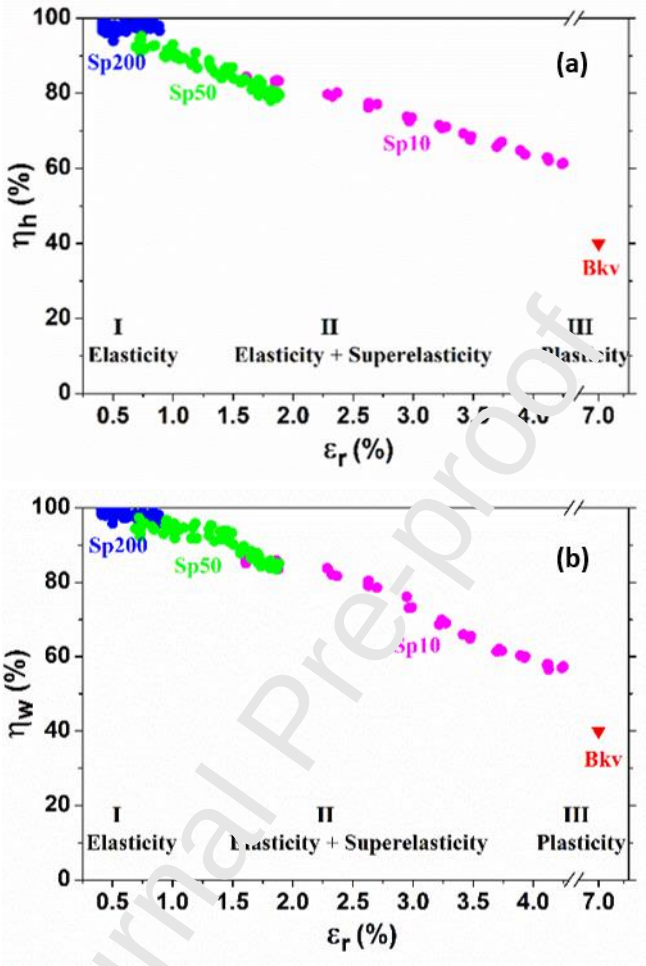

Fig. 7. Plots of the recovery ratios as a function of the calculated ε_r for the three spherical indenters Sp200, Sp50 and Sp10 and for the Bkv indenter: (a) η_h and (b) η_w.

Owing to the various indenters used in this work, ε_r was varying continuously from 0.4% to 4.3%, and thereafter up to 7%, allowing the study of the indentation response of our film through different deformation regimes. Results may be described in a three-stage evolution: (I) elastic regime; (II) elasto-plastic regime for which the response of the superelastically deformed region predominates; and (III) elasto-plastic regime with prominent plastic deformation. At low strain state ($\varepsilon_r \leqslant 1\%$), the imposed

strain was fully accommodated by the elastic deformation of the material underneath the Sp200 tip as illustrated by the complete indent recovery upon unloading shown in Fig. 8(b), on the AFM image after Sp200 indentation at h_m = 280 nm. As the imposed strain was increased (1% ≤ ε_r ≤ 4.3%), relatively large recovery ratios were observed ranging from 95% to 60%. Plastic deformation appeared to occur progressively leading to the continuous decrease of η_h and η_w ratios during Sp50 and Sp10 indentations. Figs. 8 (c)-(d)-(e)-(f) display nanoindentation imprints after Sp50 indentation (ε_r = 1.7%) and after Sp10 indentation (ε_r = 3.9%) with both at h_m = 280 nm and their corresponding depth cross-sectional profiles evidencing that for a fixed h_m, the permanent indent depth, h_p, has increased progressively with the imposed strain. It may be noted here that h_p was 50 nm for the Sp50 indentation at ε_r = 1.7% and h_p was 104 nm for the Sp10 indentation at ε_r = 3.9%. In this way, plastic deformation still remains the minor mechanism while superelastic deformation with reversible and stress-induced martensitic transformation is supposed to be the predominant deformation mechanism for ε_r between 1% and 4.3%. Subsequently, the increasing amount of dislocations has restricted additional formation of martensite upon loading and impeded the reverse transformation of the existent martensite upon unloading since the high density of dislocations stabilized both the parent β phase and the existent martensite [47]. When the local stress exceeds the yield stress of martensite, permanent deformation occurs leading to the stabilization of martensite. The stress relaxation arising from plastic deformation also reduces the driving force for phase transformation. Thus, the increasing imposed strain reduces progressively the superelastic response due to an increased volume fraction of

dislocations and stabilized martensite. When ε_r was increased to about 7% during Bkv indentations, immediate plastic deformation of parent β phase was supposed to occur beneath the tip and large permanent depths persisted upon unloading as shown in Fig. 8 (g)-(h) for which a very high residual depth of 176 nm was observed after Bkv indentation still for the same maximum depth h_m of 280 nm. The 37% of η_h recovery ratio and the 40% of η_w recovery ratio measured during Bkv indentations were contributed by the elastic strain relaxation of mainly parent β phase and some martensite from the outer region.

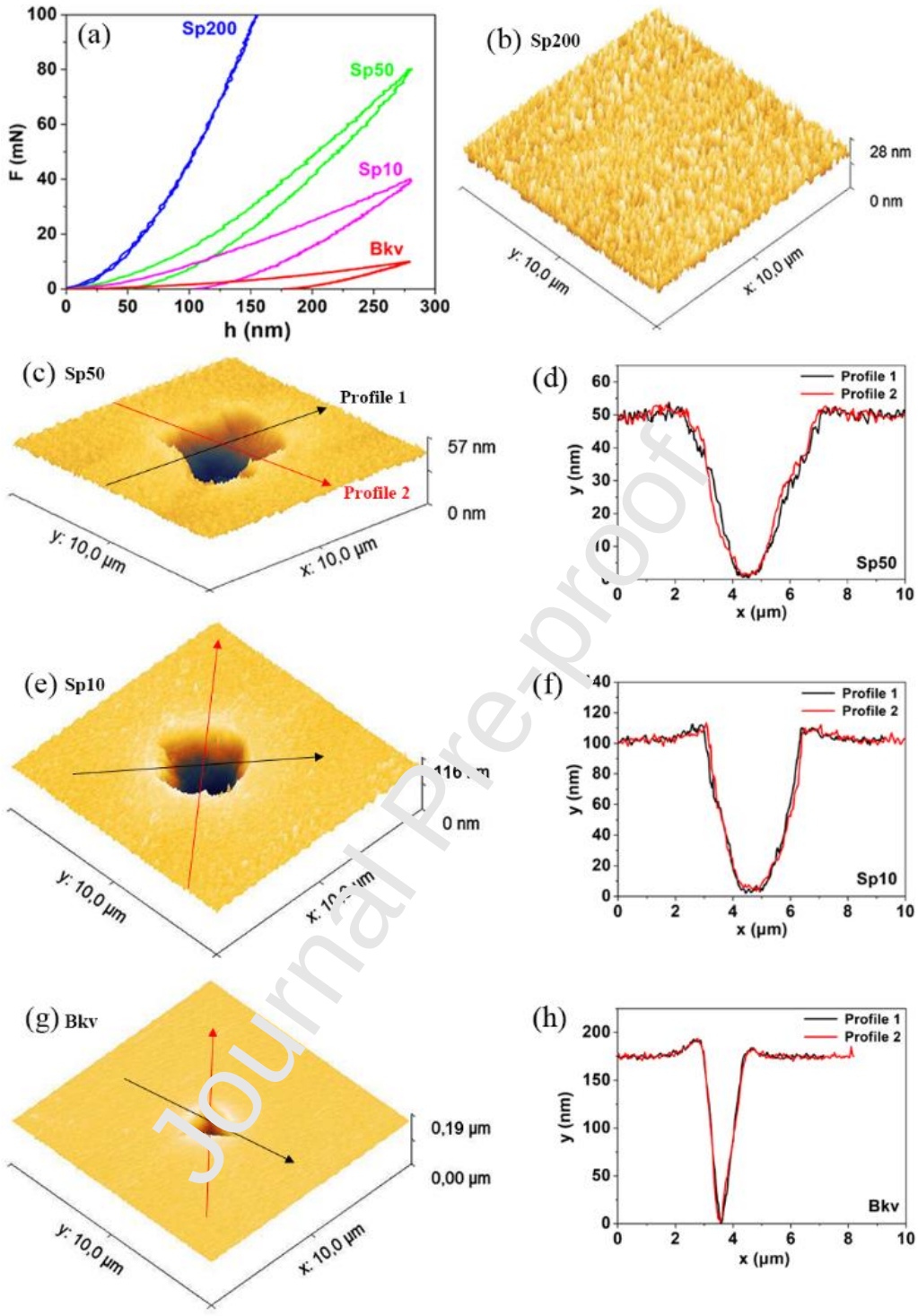

Fig. 8. Recoveries of indentation depths after indentation at h_m = 280 nm were observed using AFM: (a) for the Sp200 indenter, ε_r = 0.8% ; (b) for the Sp50 indenter, ε_r = 1.7% and (c) the corresponding depth profiles; (d) for the Sp10, ε_r = 3.9% and (e) the corresponding depth profiles; (f) for the Bkv indenter, ε_r = 7% and (g) the corresponding

depth profiles.

Until now, discussion was focused on differences in the unloading data including calculation of the recovery ratios for the various indenter geometries. Indeed, unloading curves reflect contribution of the lattice relaxation and contribution of the reverse martensitic transformation. Nevertheless, there were also significant differences in the loading portions of the raw *F-h* curves depending on the indenter geometry. Fig. 8(a) displays the raw *F-h* curves measured at h_m = 280 nm for the three Sp10, Sp50 and Sp200 spherical indenters and for the Bkv indenter. One can note that only the front end of the *F-h* curve for the Sp200 indenter is visible at the selected scale. This plot displays a clear divergence between the loading behaviors depending on the indenter geometry. Loading curves reflect accommodation of the imposed deformation primarily through elastic strains and then through phase transformation (martensite formation) and through plastic process (dislocation motion). In this way, three indentation regimes may be reappointed: (i) prominent elastic deformation of β phase with the Sp200 indenter; (ii) mainly elastic and superelastic deformations with Sp50 and Sp10 indenters; and (iii) predominant plastic deformation with Bkv indenter.

Interpreting the measured indentation response which is as such difficult for conventional elasto-plastic materials due to the complex loading conditions imposed during nanoindentation experiment involving inhomogeneous distribution of stress and strain fields underneath the indenter tip and the constantly evolving probing volume, becomes even more complex when simultaneous superelastic deformation (i.e. phase transformation) occurs in conjunction with elastic and plastic deformation. Many efforts

have been made to depict the deformation process during nanoindentation. Fischer-Cripps introduced the normalized contact stress distribution to quantitatively determine the deformation characteristics [48] and showed that the severe stress concentration beneath the sharp Bkv indenter results in larger plastic zone than under spherical indenter. The stress-affected indentation volume has approximately a spherical shape whatever the tip geometry and the affected volume under spherical indenter is significantly greater than that for Bkv indenter at the same penetration depth [49]. Crone et al. firstly illustrated the deformation process occurring beneath the indenter tip for superelastic NiTi films by a series of three concentric shells: a plastic deformation region, a stress-induced martensitic transformation region and an elastic deformation region as the stress level decays further away from the tip [50]. Maletta et al. [51] and Kan et al. [52] carried out FEM simulations to investigate the microstructural evolution due to the phase transition in the indentation region by comparing the Von Mises equivalent stress with the characteristic transformation stresses (start and finish transformation stresses) of superelastic alloys. They described the deformation process occurring beneath the indenting tip as a series of four concentric shells: a fully transformed martensite zone plastically deformed in the region nearest the indenter tip, a fully transformed and reversible martensite region further from the indenter tip, a partial transformation zone still further away from the indenter tip and a fully untransformed parent β phase zone. It has been shown that the magnitude and spatial distribution of the evolving strain field in the indentation region is strongly affected by the indenter geometry [30, 32]. The present study used four indenters with different

geometries to investigate the contribution of the superelastic response over a large range of representative strain. Fig. 9 presents an overview of our measurements coupled with a schematic representation of the evolution of the predominant deformation mechanisms with respect to the representative strain imposed and to the indenter geometry. Results showed the importance of selecting the appropriate representative strain window to reveal superelasticity. Under Bkv indenter, the response of the material is dominated by regions of high strains generated immediately under the tip and for which strain levels exceed those which can be accommodated by elastic and superelastic deformations leading to the large predominance of the plastic deformation during Berkovich indentation. Using a large spherical tip, such as the Sp200 indenter, it does not seem the most appropriate to deal with superelasticity due to the wide strain field beneath the tip which is considerably lower and promotes the prevalence of the conventional elastic deformation of the parent β phase. Indenting with intermediate spherical tip, such as Sp50 and Sp10 indenters, is a viable strategy to reveal the superelastic response of materials in the micro- and nano-meter length scales by ensuring that the straining is in the competitive regime between superelastic and plastic deformations.

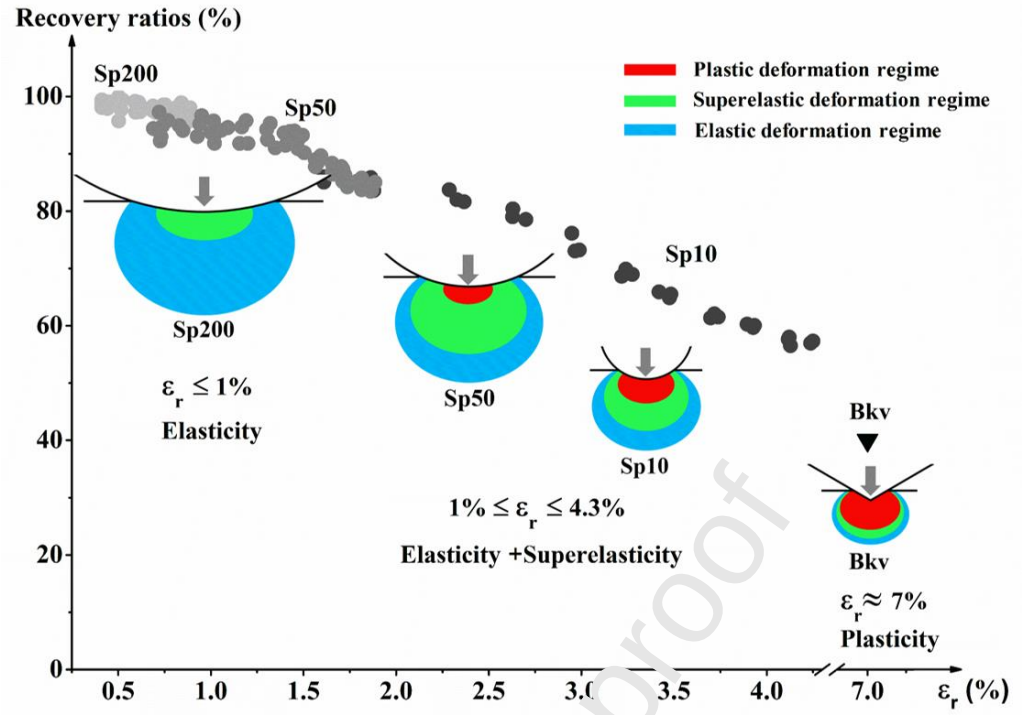

Fig. 9. Schematic representation of the prominent deformation mechanisms occurring underneath the indenter tip as the load is applied to the film surface with respect to the representative strain ε_r and to the indenter geometry.

5. Conclusion

A new Ti-16Zr-13Nb-2Sn superelastic film was elaborated by magnetron sputtering at room temperature from a single alloyed target. The film displays nanograined microstructure fully composed of metastable β phase with preferential growth orientation along [110] direction.

The superelastic response of the Ti16132 film was examined in light of nanoindentation experiments by measuring the depth and work recovery ratios from the load-displacement curves for various penetration depths. Results were discussed with regard to the calculation of the representative strain. Owing to the four different indenters employed in this work, representative strain was varying continuously from

0.4% to 4.3% using three spherical indenters with tip radii of 200 μm (Sp200), 50 μm (Sp50) and 10 μm (Sp10), and thereafter up to 7% with the Berkovich (Bkv) indenter. The nanoscale indentation behavior of Ti16132 film was significantly affected by the indenter geometry due to the large differences in the magnitude and spatial distribution of the strains developed beneath each indenter tip.

Using the Bkv indenter, almost no depth dependence of recovery ratios was observed. The constant and high representative strain (≈7%) imposed whatever the applied loads was beyond the level that can be accommodated by superelastic deformation leading to restricted recovery ratio measurements as low as 40%. Such conditions promote plastic deformation resulting in high density of dislocations which contribute to both limit the formation of martensite and inhibit its subsequent reversion to the parent β phase.

In contrast, the representative strain imposed during spherical indentations is depth dependent with respect to the indenter radius allowing to encompass the different deformation regimes from elastic to elasto-plastic regimes. Nearly 100% recovery ratios were measured with the large radius spherical indenter (Sp200) which imposed relative low representative strain ($0.4\% \leq \varepsilon_r \leq 1\%$) and probed predominately elastic deformation. Large recovery ratios ranging from 95% to 60% were measured with Sp50 and Sp10 indenters for ε_r between 1% and 4.3%. Plastic deformation is then still the minor mechanism while superelastic deformation with reversible and stress-induced martensitic transformation is the predominant deformation mechanism. Indenting with intermediate spherical tips, such as Sp50 and Sp10 indenters, is a viable strategy to

reveal the superelastic response of materials in the micro- and nano-meter length scales by ensuring that the straining is in the competitive regime between superelastic and plastic deformations.

The present work shows the importance of considering the appropriate indentation depth window associated to the indenter tip radius to reveal the superelastic behavior of materials on the nanoscale. Superelastic performance is very sensitive to the applied strain level and spherical indentations offer the opportunity to determine at the local scale the strain levels under which small volumes of material would perform superelastic deformation and recovery.

Acknowledgements

Y. Zhou acknowledges the China Scholarship Council (CSC) for her Ph.D financial support (No. 201701810085). The authors also acknowledge the SCANMAT platform of the University of Rennes for providing access to SEM and TEM facilities. This work has been partially supported by the ANR project 18-CE08-0017 Super-Rev.

References

[1] E. Eisenbarth, D. Velten, M. Müller, R. Thull, J. Breme, Biocompatibility of β-stabilizing elements of titanium alloys, Biomaterials, 25 (26) (2004), pp. 5705-5713.

[2] M. Niinomi, M. Nakai, J. Hieda, Development of new metallic alloys for biomedical applications, Acta Biomater., 8 (11) (2012), pp. 3888-3903.

[3] T. Duerig, A. Pelton, D. Stöckel, An overview of nitinol medical applications, Mater. Sci. Eng. A, 273 (1999), pp. 149-160.

[4] M.F. Ijaz, L. Héraud, P. Castany, I. Thibon, T. Gloriant, Superelastic behavior of biomedical metallic alloys, Metall. Mater. Trans. A ,51A (2020), pp. 3733-3741.

[5] A. Biesiekierski, J. Wang, M.A.-H. Gepreel, C. Wen, A new look at biomedical Ti-based shape memory alloys, Acta Biomater., 8 (5) (2012), pp. 1661-1669.

[6] P. Castany, A. Ramarolahy, F. Prima, P. Laheurte, C. Curfs, T. Gloriant, In situ synchrotron X-ray diffraction study of the martensitic transformation in superelastic Ti-24Nb-0.5 N and Ti-24Nb-0.5 O alloys, Acta Mater., 88 (2015), pp. 102-111.

[7] Y. Hao, S. Li, S. Sun, R. Yang, Effect of Zr and Sn on Young's modulus and superelasticity of Ti–Nb-based alloys, Mater. Sci. Eng. A, 441(1-2) (2006), pp. 112-118.

[8] Y. Hao, S. Li, S. Sun, C. Zheng, R. Yang, Elastic deformation behaviour of Ti–24Nb–4Zr–7.9 Sn for biomedical applications, Acta Biomater., 3(2) (2007), pp. 277-286.

[9] Y. Yang, P. Castany, M. Cornen, F. Prima, S. Li, Y. Hao, T. Gloriant, Characterization of the martensitic transformation in the superelastic Ti–24Nb–4Zr–8Sn alloy by in situ synchrotron X-ray diffraction and dynamic mechanical analysis, Acta Mater., 88 (2015), pp. 25-33.

[10] J. Fu, A. Yamamoto, H.Y. Kim, H. Hosoda, S. Miyazaki, Novel Ti-base superelastic alloys with large recovery strain and excellent biocompatibility, Acta Biomater., 17 (2015), pp. 56-67.

[11] S. Li, Y.-W. Kim, M.-S. Choi, T.-H. Nam, Superelastic Ti-18Zr-12.5Nb-2Sn (at.%) alloy scaffolds with high porosity fabricated by fiber metallurgy for biomedical applications, Intermetallics, 115 (2019), pp. 106631.

[12] J. Gao, I. Thibon, P. Castany, T. Gloriant, Effect of grain size on the recovery strain in a new Ti–20Zr–12Nb–2Sn superelastic alloy, Mater. Sci. Eng. A, 793 (2020), pp. 139878.

[13] L.L. Pavón, H.Y. Kim, H. Hosoda, S. Miyazaki, Effect of Nb content and heat treatment temperature on superelastic properties of Ti–24Zr–(8–12) Nb–2Sn alloys, Scr. Mater., 95 (2015), pp. 46-49.

[14] S. Li, T.-H. Nam, Superelasticity and tensile strength of Ti-Zr-Nb-Sn alloys with high Zr content for biomedical applications, Intermetallics, 112 (2019), pp. 106545.

[15] S. Miyazaki, A. Ishida, Martensitic transformation and shape memory behavior in

sputter-deposited TiNi-base thin films, Mater. Sci. Eng. A, 273 (1999), pp. 106-133.

[16] H. Rumpf, T. Walther, C. Zamponi, E. Quandt, High ultimate tensile stress in nano-grained superelastic NiTi thin films, Mater. Sci. Eng. A, 415(1-2) (2006), pp. 304-308.

[17] X.-G. Ma, K. Komvopoulos, Pseudoelasticity of shape-memory titanium–nickel films subjected to dynamic nanoindentation, Appl. Phys. Lett., 84(21) (2004), pp. 4274-4276.

[18] K. Li, Y. Li, K. Yu, C. Liu, D. Gibson, A. Leyland, A. Matthews, Y.Q. Fu, Crystal size induced reduction in thermal hysteresis of Ni-Ti-Nb shape memory thin films, Appl. Phys. Lett., 108(17) (2016), pp. 171907.

[19] S. Achache, S. Lamri, M.A.P. Yazdi, A. Billard, M. François, F. Sanchette, Ni-free superelastic binary Ti–Nb coatings obtained by DC magnetron co-sputtering, Surf. Coat. Technol., 275 (2015), pp. 283-288.

[20] J. Yang, M. Baatarsukh, J. Bae, S. Huh, H. Jeong, B. Choi, T. Nam, J. Noh, Phase stability and properties of Ti-Nb-Zr thin films and their dependence on Zr addition, Materials, 11(8) (2018), pp. 1361.

[21] S. Achache, S. Lamri, A. Alhussein, A. Billard, M. François, F. Sanchette, Gum Metal thin films obtained by magnetron sputtering of a Ti-Nb-Zr-Ta target, Mater. Sci. Eng. A, 673 (2016), pp. 492-502.

[22] D. Photiou, N.T. Panagiotopoulos, L. Koutsokeras, G.A. Evangelakis, G.Constantinides, Microstructure and nanomechanical properties ofmagnetron sputtered Ti−Nb film, Surf. Coat. Technol., 302 (2016), pp. 310–319 .

[23] J. Málek, V. Starý, The correlation between substrate and deposited biocompatible layer microstructures on different substrates, Appl. Surf. Sci., 459 (2018), pp. 114-119.

[24] E.D. Gonzalez, Conrado R.M. Afonso, Pedro A.P. Nascente, Influence of Nb content on the structure, morphology, nanostructure, and properties of titanium-niobium magnetron sputter deposited coatings for biomedical applications, Surf. Coat. Technol., 326 (2017), pp. 424–428.

[25] D.A. Tallarico, A.L. Gobbi, P.I. Paulin Filho, M.E.H. Maia da Costa, P.A.P. Nascente, Growth and surface characterization of TiNbZr thin films deposited by magnetron sputtering for biomedical applications, Mater. Sci. Eng. C, 43 (2014), pp. 45-49.

[26] E. Frutos, M. Karlík, J.A. Jiménez, H. Langhansová, J. Lieskovská, T. Polcar, Development of new β/α ″-Ti-Nb-Zr biocompatible coating with low Young's modulus and high toughness for medical applications, Mater. Des., 142 (2018), pp. 44-55.

[27] X.-H. Yan, J. Ma, Y. Zhang, High-throughput screening for biomedical applications in a Ti-Zr-Nb alloy system through masking co-sputtering, Science China: Physics, Mechanics & Astronomy, 62 (9) (2019), pp. 996111.

[28] J. Musil, A. Bell, J. Vlček, T. Hurkmans, Formation of high temperature phases in

sputter deposited Ti-based films below 100 C, J. Vac. Sci. Technol. A ,14 (4) (1996), pp. 2247-2250.

[29] M.F. Ijaz, H.Y. Kim, H. Hosoda, S. Miyazaki, Effect of Sn addition on stress hysteresis and superelastic properties of a Ti–15Nb–3Mo alloy, Scr. Mater., 72 (2014), pp. 29-32.

[30] A.M. Wood, T. Clyne, Measurement and modelling of the nanoindentation response of shape memory alloys, Acta Mater., 54 (20) (2006), pp. 5607-5615.

[31] R. Liu, D. Li, Y. Xie, R. Llewellyn, H. Hawthorne, Indentation behavior of pseudoelastic TiNi alloy, Scr. Mater., 41 (7) (1999), pp. 691-696.

[32] W. Ni, Y.-T. Cheng, D.S. Grummon, Microscopic shape memory and superelastic effects under complex loading conditions, Surf. Coat. Technol., 177 (2004), pp. 512-517.

[33] V. Shastry, U. Ramamurty, Simultaneous measurement of mechanical and electrical contact resistances during nanoindentation of NiTi shape memory alloys, Acta Mater., 61 (14) (2013), pp. 5119-5129.

[34] K.L. Johnson, K.L. Johnson, Contact mechanics, Cambridge university press, 1987.

[35] D. Tabor, The hardness of metals, Oxford university press, 2000.

[36] L. Min, C. Wei-Min, L. Nai-Gang, W. Ling-Dong, A numerical study of indentation using indenters of different geometry, J. Mater. Res., 19 (1) (2004), pp. 73-78.

[37] W.C. Oliver, G.M. Pharr, An improved technique for determining hardness and elastic modulus using load and displacement sensing indentation experiments, J. Mater. Res., 7 (6) (1992), pp. 1564-1583.

[38] S. Habib, A. Rizk, I. Mousa, Physical parameters affecting deposition rates of binary alloys in a magnetron sputtering system, Vacuum, 49 (2) (1998), pp. 153-160.

[39] Y. Yamamura, H. Tawara, Energy dependence of ion-induced sputtering yields from monatomic solids at normal incidence, At. Data Nucl. Data Tables, 62 (2) (1996), pp. 149-253.

[40] X. Feng, G. Tang, M. Sun, X. Ma, L. Wang, K. Yukimura, Structure and properties of multi-targets magnetron sputtered ZrNbTaTiW multi-elements alloy thin films, Surf. Coat. Technol., 228 (2013), pp. S424-S427.

[41] J. Pelleg, L. Zevin, S. Lungo, N. Croitoru, Reactive-sputter-deposited TiN films on glass substrates, Thin Solid Films, 197(1-2) (1991), pp. 117-128.

[42] B. Rauschenbach, J. Gerlach, Texture development in titanium nitride films grown by low-energy ion assisted deposition, Cryst. Res. Technol., 35 (6-7) (2000), pp. 675-688.

[43] H. Jabir, A. Fillon, P. Castany, T. Gloriant, Crystallographic orientation dependence of mechanical properties in the superelastic Ti-24Nb-4Zr-8Sn alloy, Phys. Rev. Mater., 3 (6) (2019), pp. 063608.

[44] Y. Zhang, Y.-T. Cheng, D.S. Grummon, Finite element modeling of indentation-induced superelastic effect using a three-dimensional constitutive model for shape memory materials with plasticity, J. Appl. Phys., 101 (5) (2007), pp. 053507.

[45] G.A. Shaw, D.S. Stone, A.D. Johnson, A.B. Ellis, W.C. Crone, Shape memory effect in nanoindentation of nickel–titanium thin films, Appl. Phys. Lett., 83 (2) (2003), pp. 257-259.

[46] J. Čech, P. Haušild, O. Kovářík, A. Materna, Examination of Berkovich indenter tip bluntness, Mater. Des., 109 (2016), pp. 347-353.

[47] J. Anuja, R. Narasimhan, U. Ramamurty, Effects of superelasticity and plasticity on the spherical indentation response of shape memory alloys: a finite element analysis, Smart Mater. Struct., 28 (3) (2019), pp. 035028.

[48] A.C. Fischer-Cripps, Introduction to contact mechanics, Springer, 2007.

[49] V. Králík, J. Němeček, Comparison of nanoindentation techniques for local mechanical quantification of aluminium alloy, Mater. Sci. Eng. A, 618 (2014), pp. 118-128.

[50] W. Crone, G. Shaw, D. Stone, A. Johnson, A. Ellis, Shape recovery after nanoindentation of NiTi thin films, Proceedings of the SEM Annual Conference on Experimental Mechanics, Citeseer, 2003.

[51] C. Maletta, F. Furgiuele, E. Sgambitterra, M. Callisti, B. Mellor, R. Wood, Indentation response of a NiTi shape memory alloy: modeling and experiments, Frattura ed Integrità Strutturale, 6 (21) (2012), pp. 5-12.

[52] Q. Kan, W. Yan, G. Kang, Q. Sun, Oliver–Pharr indentation method in determining elastic moduli of shape memory alloys—a phase transformable material, J. Mech. Phys. Solids, 61 (10) (2013), pp. 2015-2033.

Declaration of interests

☒ The authors declare that they have no known competing financial interests or personal relationships that could have appeared to influence the work reported in this paper.

☐The authors declare the following financial interests/personal relationships which may be considered as potential competing interests:

Highlights

β-Ti-Zr-Nb-Sn films were obtained by magnetron sputtering.
Nanoscale microstructure was observed in the films.
Films displayed superelastic properties.
Nanoindentation was used to investigate the superelastic response of films.
The locally superelastic responses depend on the indenter geometry and loading conditions.